Earth and Planetary Science Letters 541 (2020) 116293

Contents lists available at ScienceDirect

Earth and Planetary Science Letters

www.elsevier.com/locate/epsl

Atmospheric river changes shaped mid-latitude hydroclimate since the mid-Holocene

Christopher B. Skinner [a,*], Juan M. Lora [b], Ashley E. Payne [c], Christopher J. Poulsen [d]

[a] Department of Environmental, Earth and Atmospheric Sciences, University of Massachusetts Lowell, Lowell, MA, USA
[b] Department of Geology and Geophysics, Yale University, New Haven, CT, USA
[c] Department of Climate and Space Sciences and Engineering, University of Michigan, Ann Arbor, MI, USA
[d] Department of Earth and Environmental Sciences, University of Michigan, Ann Arbor, MI, USA

ARTICLE INFO

Article history:
Received 16 September 2019
Received in revised form 17 April 2020
Accepted 19 April 2020
Available online 6 May 2020
Editor: L. Robinson

Keywords:
atmospheric river
Holocene climate
climate change
precipitation

ABSTRACT

Paleoclimate proxies indicate that changes in insolation since the mid-Holocene have driven widespread hydrologic changes across the midlatitudes. It is unclear how atmospheric rivers (ARs), which are fundamental to global moisture transport today, may have contributed to these Holocene hydroclimate changes. Here, we use a set of climate model simulations with the Community Earth System Model (CESM), and introduce an AR algorithm optimized to identify ARs within different climate states, to show that changes to the location and intensity of landfalling ARs explain the majority of the precipitation difference between the mid-Holocene and the preindustrial period in several midlatitude regions. During the mid-Holocene, enhanced seasonality increased summer season AR vapor content and displaced ARs poleward of their preindustrial period trajectories, especially in the Northern Hemisphere. Consequently, in high midlatitude coastal areas of western North America and East Asia, ARs account for greater than 10% more of total precipitation during the mid-Holocene, and nearly 100% of the simulated change in precipitation between the two climates. The simulated AR changes are consistent with moisture-sensitive proxy records and with present-day relationships between ARs and regional circulation, enhancing confidence that ARs served as the underlying synoptic mechanism responsible for mid-Holocene hydroclimate anomalies in several coastal mid-latitude areas. The results indicate that ARs are sensitive to background climate state, and suggest that changes in ARs may have contributed to hydroclimate changes throughout Earth's past.

1. Introduction

The mid-latitude atmosphere is punctuated by fast-moving conduits of highly concentrated water vapor transport known as atmospheric rivers (ARs). These relatively narrow synoptic features, commonly less than 1,000 km in width, form over oceans often within the warm sectors of extratropical cyclones (Ralph et al., 2004) and serve as key pathways for the transport of moisture and latent heat from low to mid latitudes and from oceans to land (Zhu and Newell, 1998). The moisture transport in an AR is often disrupted when the AR makes landfall. Aided by near-moist neutral stratification within the AR, AR landfalls can lead to exceptionally high precipitation totals, particularly in regions of elevated terrain (Neiman et al., 2008; Rutz et al., 2014). In the present climate, ARs contribute between 30% – 50% of annual water supply along mid-latitude western continental boundaries, including western North America, Europe, Chile, and South Africa (Guan and Waliser, 2015; Lavers and Villarini, 2015; Blamey et al., 2017; Viale et al., 2018), most of which occurs in just a handful of AR events each year (Guan et al., 2010). Consequently, even small changes in the frequency and location of ARs have implications for regional climate and ecosystem vitality (Albano et al., 2017). While the majority of AR research to date has focused on understanding how these AR changes shape modern and future hydroclimate (e.g., Payne and Magnusdottir, 2015; Shields and Kiehl, 2016), it is highly likely ARs also contributed to hydroclimate changes in Earth's recent and distant past (Lora et al., 2017; Kiehl et al., 2018).

Although direct evidence for past AR activity within paleoclimate proxy records is generally not available, there is an abundance of moisture sensitive proxies that suggest widespread hydrologic changes during the Holocene (~11.5 ka B.P. to the present) in regions that currently experience ARs. Lake sediments, speleothems, and pollen records from the mid-Holocene indicate

* Corresponding author at: University of Massachusetts Lowell, 265 Riverside St, Lowell, MA 01854, USA.
E-mail addresses: christopher_skinner@uml.edu (C.B. Skinner), juan.lora@yale.edu (J.M. Lora), aepayne@umich.edu (A.E. Payne), poulsen@umich.edu (C.J. Poulsen).

https://doi.org/10.1016/j.epsl.2020.116293

Table 1
CESM boundary forcings.

Simulation	CO_2	CH_4	N_2O	Solar	Ecc	Obliq	Prec
CESM-PI	284 ppm	760 ppb	270 ppb	1365 $W\,m^{-2}$	0.016724	23.446°	102.04°
CESM-MH	280 ppm	650 ppb	270 ppb	1365 $W\,m^{-2}$	0.018682	24.105°	0.87°
CESM-EH	266 ppm	688 ppb	263 ppb	1365 $W\,m^{-2}$	0.019419	24.227°	294.82°

drier than present conditions along the U.S. west coast from California to Washington (Bartlein et al., 2011; Hermann et al., 2018), and wetter than present conditions along western Canada and portions of Alaska (Viau and Gajewski, 2009; Steinman et al., 2016), regions that receive between 20% – 40% of their total annual rainfall from ARs today (Guan and Waliser, 2015). Proxies indicate a similar equatorward shift in precipitation since the mid-Holocene in East Asia (Herzschuh et al., 2019), a region that currently experiences frequent AR landfalls during summer months (Kamae et al., 2017), and in central and southern Chile (Lamy et al., 2010), which average 35 – 40 days of AR landfalls per year (Viale et al., 2018). Additionally, the Northeast U.S. and southeastern Canada, which receive an estimated 20% – 30% of present-day total annual rainfall from ARs (Lavers and Villarini, 2015), were considerably drier during the mid-Holocene (Bartlein et al., 2011). Several of these past mid-latitude hydrologic responses have been attributed to orbital insolation-driven changes in the strength and position of the Northern Hemisphere jet stream and semi-permanent pressure systems (Hermann et al., 2018; Herzschuh et al., 2019; Routson et al., 2019), pointing to a potential key role of ARs as the underlying synoptic mechanism. However, to date, an explicit evaluation of ARs within a Holocene paleoclimate context has not been undertaken, limiting our interpretation of climate signals recorded in various paleoclimate proxies from this time.

Relationships between the large-scale controls on ARs and radiative forcing suggest that AR characteristics likely differ based on background climate state. Indeed, model simulations of projected future high-CO_2 climates exhibit regional shifts in AR landfall locations in response to extratropical storm track changes and increased AR vapor content due to warmer air and sea surface temperatures (Gao et al., 2015; Payne and Magnusdottir, 2015; Shields and Kiehl, 2016). Altered insolation seasonality during the Holocene has also been shown to influence temperatures and atmospheric circulation at regional and global scales (Wanner et al., 2008; Routson et al., 2019), and is therefore a likely driver of AR variability on millennial time scales.

To test the hypothesis that changes in ARs shaped millennial-scale hydrologic change during the Holocene, and to quantify the sensitivity of ARs to orbital forcing, we introduce and apply a new AR identification and tracking algorithm designed to facilitate comparison of AR characteristics across different climate states to a set of Holocene climate model simulations. The details of the model simulations and AR algorithm are presented in section 2, the response of ARs to Holocene forcings is presented in section 3, and a discussion of the findings within the context of paleoclimate proxy records and previous climate modeling experiments is presented in section 4.

2. Data and methods

2.1. Climate model simulations

We use the Community Earth System Model version 1.2 (CESM1.2) (Hurrell et al., 2013) to simulate mid-Holocene *CESM-MH* (6 ka B.P.) and preindustrial *CESM-PI* (year 1850) climates. Our configuration of CESM1.2 uses the Community Atmosphere Model version 5 (CAM5), the Community Land Model version 4.5 (CLM4.5), the Community Ice Code version 4 (CICE4), and the Parallel Ocean Program version 2 (POP2). The atmosphere and land models are run on a 0.9° × 1.25° finite volume grid. The ocean and sea ice models are run at a nominal 1° resolution.

The ocean model in each simulation is initialized from the same equilibrated ocean state. Each simulation is then run until climate equilibration is reached under orbital and greenhouse gas conditions consistent with each time period (Table 1) (Berger et al., 1993; Monnin et al., 2001). The major difference between *CESM-MH* and *CESM-PI* is the orbital precession, which alters the timing of perihelion and therefore the seasonality of solar insolation. During the mid-Holocene, perihelion coincided with Northern Hemisphere summer, intensifying summer insolation in the Northern Hemisphere relative to the preindustrial period. We analyze the final 50 years of data after equilibration in each simulation.

To account for the presence of widespread vegetation in northern Africa and the Arabian Peninsula during the mid-Holocene (Hoelzmann et al., 1998)—which has been shown to exert a global-scale influence on temperature, circulation, and precipitation (Davies et al., 2015; Claussen et al., 2017)—a mix of tropical grasses, broadleaf deciduous trees and broadleaf deciduous shrubs, as well as a darker soil color (with dry and saturated soil albedos of 0.18 and 0.09, respectively) is prescribed over 6°N–36°N, 20°W–65°E in *CESM-MH*. Outside of northern Africa and the Arabian Peninsula, the distribution of plant functional types in the two simulations is identical and set to modern day values. The carbon and nitrogen cycle model, which regulates leaf and stem area index, is active in *CESM-PI*, but is inactive in *CESM-MH* (leaf and stem area index are prescribed) to prevent vegetation mortality in northern Africa and the Arabian Peninsula, a common problem in mid-Holocene simulations with dynamic vegetation or carbon and nitrogen cycling turned on (Hopcroft et al., 2017).

To further test the sensitivity of AR changes to the seasonality of Holocene insolation, we run an additional simulation, *CESM-EH*, which is identical to *CESM-MH*, except that orbital parameters and greenhouse gas concentrations are set to early Holocene conditions (10 ka B.P.) (Table 1). *CESM-EH* utilizes the same present-day ice sheet distributions used in *CESM-PI* and *CESM-MH* and therefore does not reflect the full set of environmental conditions that likely shaped ARs during the early Holocene. As such, *CESM-EH* is used simply to assess the robustness of the AR responses to insolation forcing. We use the permutation test to assess the statistical significance of the differences between *CESM-PI* and the *CESM-MH* and *CESM-EH* simulations at the 95% confidence level.

2.2. Atmospheric river identification and tracking algorithm

We identify and characterize ARs in the model data using an automated identification algorithm based on that of Lora et al. (2017). In accordance with the AMS Glossary definition (Ralph et al., 2018), ARs are detected based on the column integrated vapor transport (IVT), which is computed as

$$IVT = \frac{1}{g}\int_{p_s}^{0} \boldsymbol{u} q dp$$

where $\boldsymbol{u}$, q, and p are the horizontal winds, specific humidity, and pressure at each vertical model level, respectively, and g and p_s are the acceleration due to gravity and the surface pressure.

ARs are defined as contiguous regions, exceeding 2000 km in length, within which IVT exceeds a latitudinally-dependent threshold value that depends on the background zonal-mean integrated water vapor (IWV). Specifically, ARs occur where

$$IVT \geq IVT_{min}\left(1 - \frac{\overline{IWV}}{\max(\overline{IWV})}\right)^{-1}$$

where $\overline{IWV}$ is the 30-day running mean of the zonally-averaged IWV, and IVT_{min} is 225 $kg\,m^{-1}\,s^{-1}$. This formulation ensures that, at high mid-latitudes in the modern climate, the threshold IVT approximates the threshold values used in various prior AR studies and in the recent AR category scale (Rutz et al., 2014; Ralph et al., 2019), while at the same time allowing the algorithm to both disregard high-moisture tropical regions and identify high latitude ARs associated with zonally-anomalous but relatively low-magnitude IVT (Gorodetskaya et al., 2014).

Importantly, our AR detection algorithm incorporates advantageous features of both absolute and relative AR detection methods (see Shields et al., 2018; Rutz et al., 2019), and takes into consideration characteristics of the background climate state. First, ARs of comparable magnitudes in the mid-latitudes are identified similarly regardless of background climate, so application of, for instance, the AR category scale (Ralph et al., 2019) is meaningful, and average AR properties like size and duration can be compared across climates. At the same time, climate-dependent—and, indeed, seasonally-dependent—features like the position and width of the intertropical convergence zone are inherently incorporated, so a warmer atmosphere does not simplistically translate to higher rates of detection at low latitudes. These attributes enable the use of a single algorithm across various climate states, ensuring the objectivity of the resulting comparison.

The AR algorithm is run on 6-hourly output from the CESM simulations. AR frequencies at each grid box (Fig. 1) are calculated based on the number of 6-hourly time steps in which an AR is detected during a specified time period divided by the total number of time steps during that time period (note, this is different from the number of individual AR events at each grid box). AR precipitation is calculated by summing the precipitation that occurred during the 6-hour time period in which the AR was detected. We evaluate the simulation of atmospheric rivers in CESM by comparing the *CESM-PI* simulation with data from years 1980 – 2016 in the Modern-Era Retrospective analysis for Research and Applications, version 2 (MERRA-2) reanalysis (Gelaro et al., 2017). MERRA-2 data is archived at a 3-hourly resolution on a 0.5° × 0.625° grid.

3. Results

3.1. Simulated preindustrial and reanalysis ARs

Application of the AR algorithm to the *CESM-PI* simulation and MERRA-2 reanalysis data reveals five distinct global hotspots of AR activity (Figs. 1a, 1b, and S1). On an annual timescale, ARs are most frequently present between 35°N/S and 55°N/S in the Pacific, Atlantic, and Indian Ocean basins. These areas of heightened AR activity extend east and west from the oceans to western and eastern North America, Western Europe, East Asia, southern South America, southern Australia, and New Zealand. Annual mean AR detection frequencies (percentage of total time steps per year in which an AR is detected within a grid cell) peak at just over 30% in the North Atlantic and between 20% and 30% in other ocean basins. Over land, ARs are detected in 0% – 12% of total timesteps, with the highest totals found in eastern North America and Northwestern Europe, consistent with the findings of Guan and Waliser (2015). Seasonally, ARs peak during the winter season in coastal

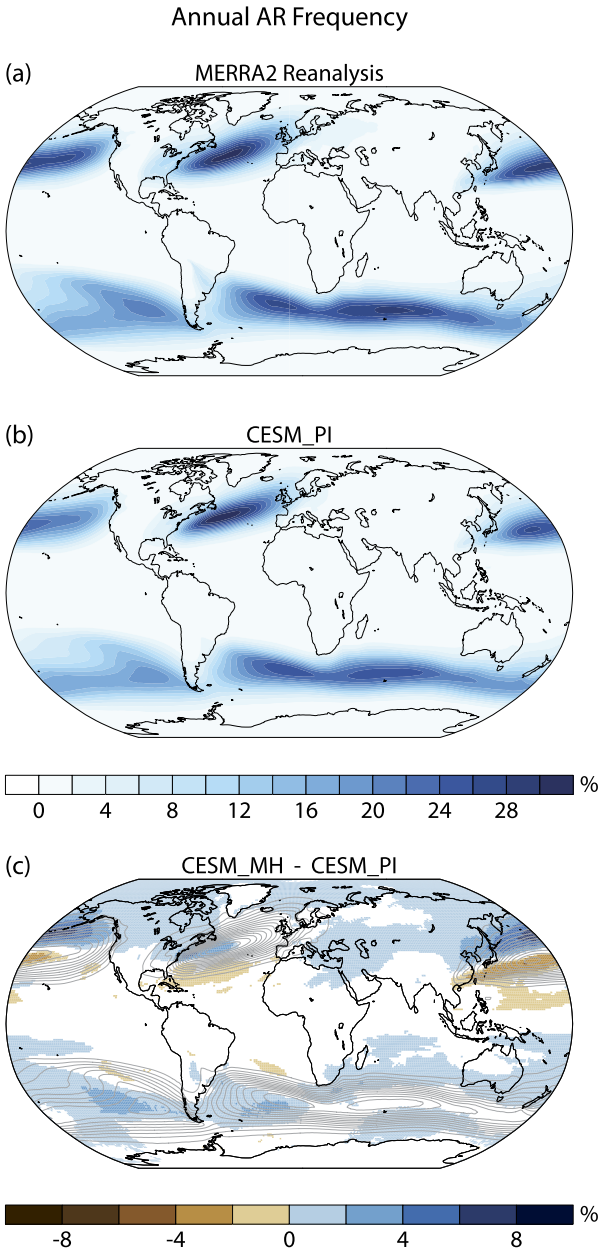

Fig. 1. (a-b) Annual mean AR frequency (percentage of timesteps with an AR) in (a) MERRA2 Reanalysis (years 1980 - 2016) and (b) CESM_PI. (c) Change in the annual mean AR frequency between CESM_MH and CESM_PI (shading). AR frequency contours from (b) are overlain on (c). Grid cells that do not exhibit statistically significant changes in (c) are shaded white. (For interpretation of the colors in the figure(s), the reader is referred to the web version of this article.)

areas of the Western and Eastern U.S., Western Canada, Western Europe, and subtropical South America, and during the summer season in portions of coastal Alaska, East Asia, and far southern Chile (Fig. S1). In general, the frequency of AR detections is slightly lower in *CESM-PI* than in MERRA-2, especially over land areas, though differences in the background climate state between the preindustrial *CESM-PI* and late 20th century MERRA-2 datasets likely contribute to the discrepancy.

3.2. AR response to Holocene insolation forcing

A comparison of zonal-mean AR characteristics in *CESM-PI* and *CESM-MH* reveals that maximum zonal-mean AR meridional IVT is greater during the mid-Holocene than in the preindustrial period

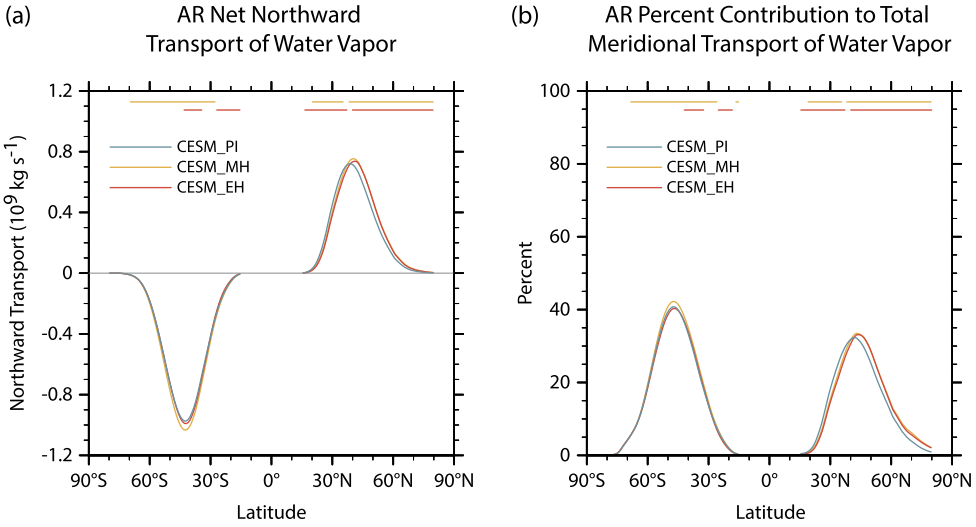

Fig. 2. (a) Annual mean net meridional transport of moisture by ARs. (b) Annual mean percent of total meridional moisture transported by ARs. Latitudes between 15°S and 15°N, and latitudes poleward of 80°N/S are masked. Statistically significant differences between CESM_PI and the CESM_EH (red) and CESM_MH (orange) simulations are marked by the colored lines at the top of each panel.

(Fig. 2a). In *CESM-PI*, zonal mean IVT peaks at a value of -0.97×10^9 kg s^{-1} in the Southern Hemisphere (note a negative value indicates southward transport) and 0.72×10^9 kg s^{-1} in the Northern Hemisphere. In *CESM-MH*, peak values are -1.03×10^9 kg s^{-1} in the Southern Hemisphere and 0.75×10^9 kg s^{-1} in the Northern Hemisphere, representing 6.2% and 4.2% increases in each hemisphere respectively. These AR moisture transport changes are consistent with an overall increase in atmospheric moisture content during the mid-Holocene, particularly in the Northern Hemisphere (Fig. S2). However, the maximum percent contribution of ARs to total zonally-integrated meridional IVT also increases slightly, indicating that ARs account for a proportionally higher amount of total water vapor transport during the mid-Holocene (Fig. 2b). In *CESM-PI* the maximum AR contribution to total zonally-integrated meridional IVT peaks at 40.8% in the Southern Hemisphere, and 32.3% in the Northern Hemisphere. In *CESM-MH*, peak values are 42.2% in the Southern Hemisphere and 33.5% in the Northern Hemisphere. The zonal-mean plots also reveal that the mid-Holocene increases in peak zonally-integrated AR moisture transport are accompanied by meridional shifts in AR activity.

In the mid-Holocene *CESM-MH* simulation, Northern Hemisphere ARs are displaced poleward (Figs. 1c and 2a and 2b). In the Northern Hemisphere, the latitude of maximum zonally-integrated meridional IVT from ARs moves from 38°N in *CESM-PI* to 41°N in *CESM-MH* (Fig. 2a). The poleward shift is most pronounced in the North Pacific where 4% reductions in the annual mean frequency of AR occurrence between 30°N and 40°N are more than compensated by increases in the annual mean frequency of AR occurrence of up to 8% at 50°N (Fig. 1c). The greatest reductions in mid-Holocene North Pacific AR frequency are located directly within the region of maximum AR activity in the preindustrial climate. Meanwhile, the greatest increases in mid-Holocene North Pacific AR frequency are located nearly 20° north of the core of preindustrial AR activity. In the North Atlantic, South Atlantic, and South Pacific, mid-Holocene AR frequency is enhanced along and just poleward of the preindustrial climate core of maximum AR activity and reduced along its equatorward flank. The shift in AR activity is consistent with a poleward shift in the Northern Hemisphere mid-latitude westerlies, especially in the Pacific, and a strengthening and displacement of boreal summer and fall mid-latitude semi-permanent anticyclones, both of which help to steer extratropical cyclones and the associated ARs (Fig. 3). Similar patterns of annual AR frequency change are found in response to the early Holocene insolation forcing in *CESM-EH*, though reduced AR activity in portions of the Southern Ocean are unique to the early Holocene insolation simulation (Fig. S3).

Over land, mid-Holocene changes in AR frequency are more pronounced and widespread at the seasonal scale (Figs. 3a-d). During boreal winter, increases in AR frequency of up to 4% are located in British Columbia, the U.S. Pacific Northwest, the U.S. east coast, and southern Chile and Argentina (Fig. 3a). In boreal spring, AR changes are greatest in East Asia, where frequency decreases by as much as 8% over southern China and increases by as much as 4% over Japan (Fig. 3b). Increases in AR frequency of 4% to 10% are present during boreal summer and fall across Alaska, British Columbia, eastern North America, East Asia, and southern Chile and Argentina (Figs. 3c and 3d). Given the impact variations in AR frequency have on precipitation totals, these terrestrial AR changes have the potential to exert a key influence on simulated precipitation differences between *CESM-MH* and *CESM-PI*.

3.3. AR driven changes in precipitation

Differences in annual mean precipitation between *CESM-MH* and *CESM-PI* are widespread (Fig. 4a) and largely agree with those inferred from various paleoclimate proxies. In the tropics, precipitation is enhanced in the northern hemisphere summer monsoon regions of northern Africa and India by as much as 900 mm yr^{-1}, and reduced in the Amazon by as much as 300 mm yr^{-1}, consistent with the orbital monsoon hypothesis (Kutzbach, 1981) and paleobotanic and paleohydrologic data (Mayle and Power, 2008; Dallmeyer et al., 2013). Drier than present conditions throughout much of the central and western United States, western Europe, subtropical South America, and southern China and wetter conditions along western Canada, the Aleutian Islands, southern Chile, and northern China also match climate reconstructions from the mid-Holocene, suggesting that *CESM-MH* can be used to study mid-Holocene precipitation processes (Lamy et al., 2010; Viau and Gajewski, 2009; Bailey et al., 2018; Hermann et al., 2018; Herzschuh et al., 2019).

An analysis of AR-derived precipitation in each simulation reveals that changes in ARs are key contributors to mid-latitude precipitation change since the mid-Holocene (Figs. 4b and 4c). Consistent with changes in AR frequency, AR precipitation increases across northwestern North America, the U.S. Great Lakes, eastern Canada, the Eastern Mediterranean, northern China, northern

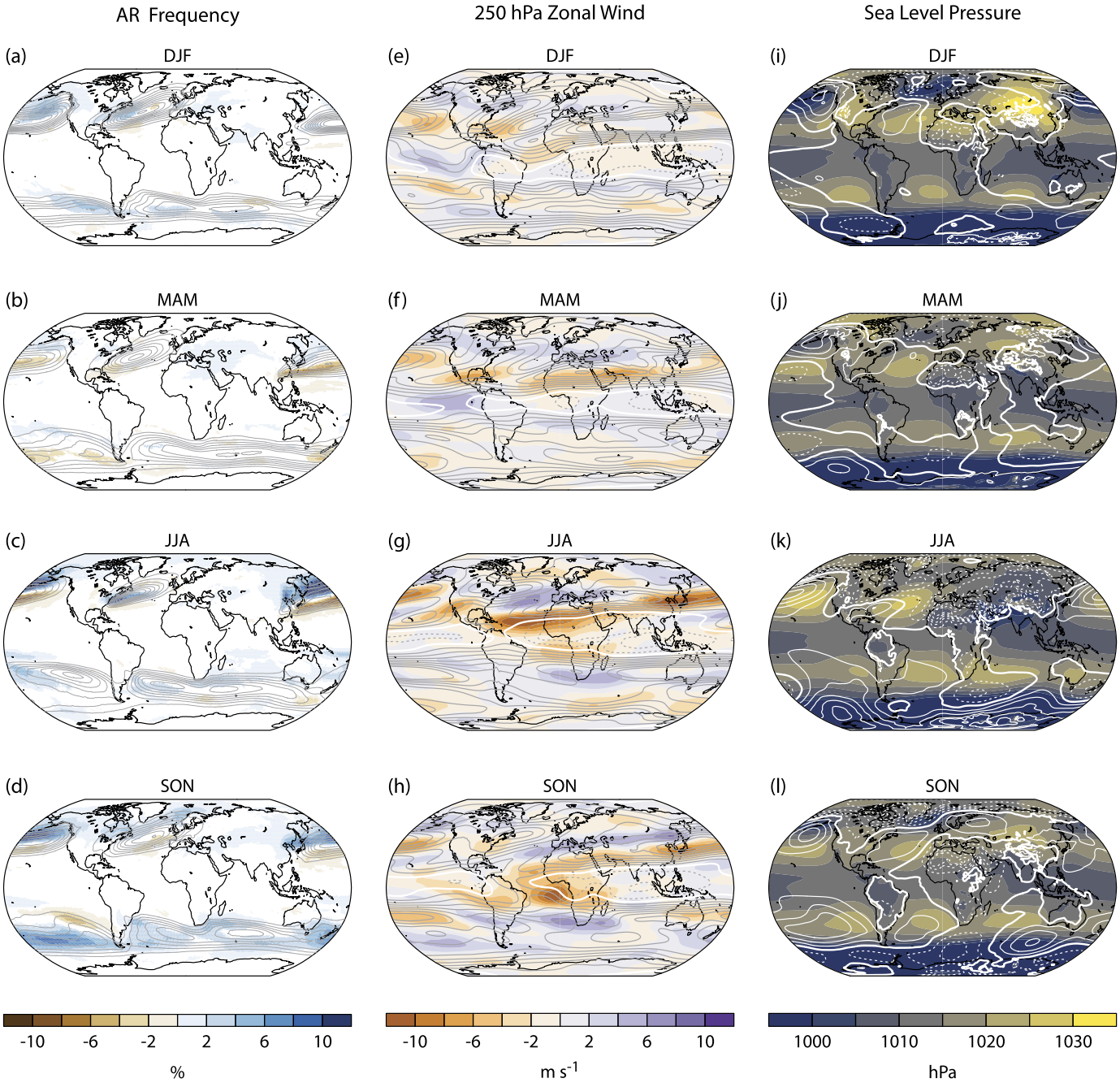

Fig. 3. (a-d) Seasonal mean AR frequency (percentage of timesteps with an AR) in CESM_PI (contours) and change in AR frequency between CESM_MH and CESM_PI (shading). (e-h) Seasonal mean 250 hPa zonal winds (contours) and change in 250 hPa zonal winds between CESM_MH and CESM_PI (shading). (i-l) Sea level pressure in CESM_PI (shading) and change in sea level pressure between CESM_MH and CESM_PI (contours). Negative contours are marked with dashed lines in (e-l). The zero contour is marked by the thick white line in (e-l). Grid cells that do not exhibit statistically significant changes in (a-d) are shaded white.

Japan, northeast Russia, southern Chile, and New Zealand during the mid-Holocene (Fig. 4b). The greatest absolute increases, in excess of 200 mm yr^{-1}, are located along coastal British Columbia, Alaska, and eastern China. In these regions, ARs account for greater than 10% more of total annual precipitation during the mid-Holocene than in the preindustrial period and are responsible for nearly the entirety of simulated precipitation differences between *CESM-MH* and *CESM-PI* (Fig. 4c). Annual mean precipitation from ARs decreases by up to 80 mm yr^{-1} in portions of the Iberian Peninsula, and by as much as 160 mm yr^{-1} in southeast China, and southern Japan, where ARs contribute about 6% less to total annual precipitation during the mid-Holocene and are responsible for the majority of the simulated precipitation difference between the simulations (Figs. 4b and 4c).

Seasonal precipitation analysis reveals that much of the AR-derived precipitation changes in Alaska, northern British Columbia, and East Asia occur during the boreal summer and fall (Fig. 5). In the Southern Andes, AR precipitation changes most during austral spring and summer, though notable decreases in mid-Holocene AR precipitation occur during austral winter in subtropical Chile. Along the Western U.S., AR precipitation changes are greatest in boreal winter, forming a north-south precipitation anomaly dipole: in the coastal southwest, decreases in mid-Holocene AR precipitation contribute to winter drying, while in the coastal northwest,

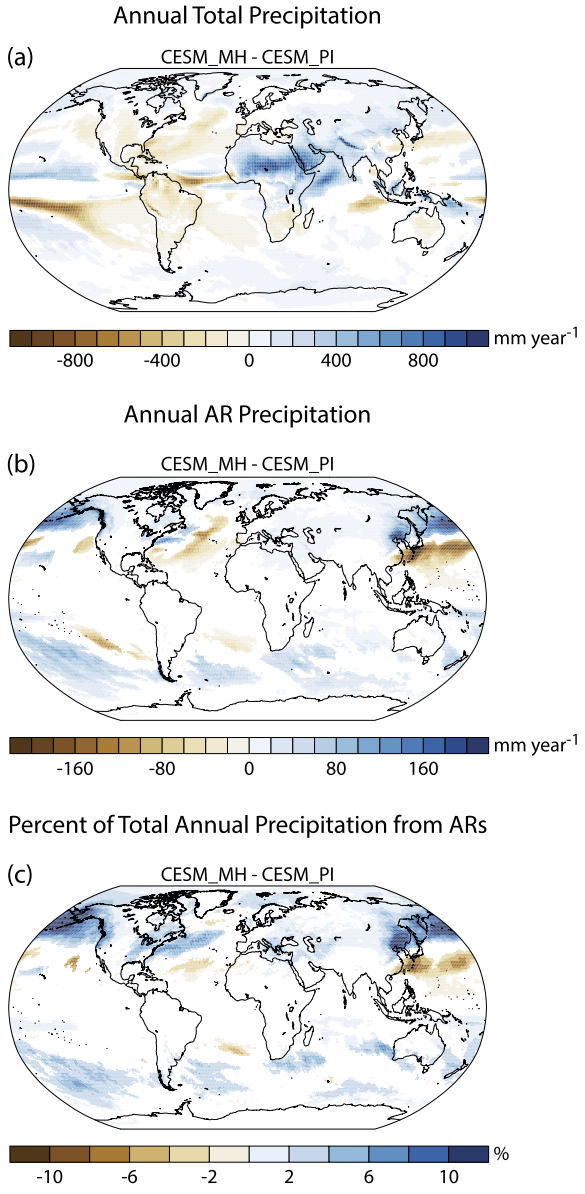

Fig. 4. (a) Change in annual total precipitation between CESM_MH and CESM_PI. (b) Change in annual AR-derived precipitation between CESM_MH and CESM_PI. (c) Change in the percent of annual total precipitation from ARs between CESM_MH and CESM_PI. Grid cells that do not exhibit statistically significant changes are shaded white.

ARs increase mid-Holocene winter precipitation (Fig. 5). Similar AR-driven precipitation changes are found in *CESM-EH*, highlighting the robust AR response to early and mid-Holocene insolation forcing (Fig. S4).

4. Discussion and conclusions

The differences in AR characteristics between the preindustrial and mid-Holocene climate simulations highlight the sensitivity of ARs to insolation forcing and point to the key role of ARs in shaping Holocene coastal mid-latitude hydroclimate change. The simulations indicate that, between the mid-Holocene and the preindustrial period, the intensity of ARs collectively weakened in the Northern and Southern Hemispheres (with regards to IVT), and shifted equatorward, especially in the Northern Hemisphere (Figs. 1c, 2, and 3a-d). These changes reduced average annual AR-derived precipitation in the high midlatitudes (poleward of ~45°) and increased precipitation at lower midlatitudes (Figs. 4 and 5). The AR changes account for the majority of the annual mean precipitation difference between the simulations in several mid-latitude regions, including northwest North America, East Asia, and southern Chile (Figs. 4a and 4b), and provide a plausible explanation for the mid to late Holocene hydroclimate changes recorded in climate proxies from these areas.

Differences in AR frequency, AR vapor transport, and AR precipitation between the CESM simulations are driven by enhanced atmospheric moisture content and regional changes in semi-permanent atmospheric pressure systems and mid-latitude storm tracks between the mid-Holocene and preindustrial period. The AR changes are most pronounced in boreal summer and fall when greater mid-Holocene insolation preferentially warms the Northern Hemisphere (Wanner et al., 2008), shifting the Intertropical Convergence Zone, Hadley Cell, and monsoon circulations poleward relative to the preindustrial (Schneider et al., 2014). The warmer mid-Holocene temperatures enhance saturation vapor pressure in the mid latitudes, increasing the moisture available to Northern Hemisphere ARs (Figs. 2 and S2). Meanwhile, intensified Southeast Asian and African monsoons during the mid-Holocene (Kutzbach, 1981) strengthen and displace the semi-permanent summer North Pacific and Bermuda High pressure systems northwestward via remote diabatic heating (Figs. 3k and 3l) (Mantsis et al., 2013). The poleward displaced Hadley cell likely helps to drive a poleward shift in the North Pacific mid-latitude storm track (Figs. 3g and 3h) (e.g. Mbengue and Schneider, 2018), and the associated intensification of the southern branch of the Hadley cell contributes to a strengthened South Pacific High during austral winter and spring (June – November), consistent with enhanced upwelling and cooler SSTs recorded in mid-Holocene isotopic data along the Chilean and Peruvian coasts (Figs. 3k and 3l) (Carré et al., 2012). In the Northern Pacific basin, these circulation changes drive a northward displacement of mid-Holocene boreal summer and fall ARs (Figs. 3c and 3d). In the Southern Pacific and Northern Atlantic basins, mid-Holocene boreal summer and fall AR frequency increases along the poleward-directed winds of the strengthened South Pacific High (southwest quadrant) and Bermuda High (northwest quadrant) (Figs. 3c, 3d, 3k, and 3l).

Though AR differences in boreal winter and spring are less widespread, these changes have important implications for hydroclimate in regions dominated by cool season precipitation such as the Western U.S. (see discussion below). The Northern Hemisphere cool season AR changes primarily consist of northward shifts in AR frequency in the northeast Pacific and northwest Atlantic (Figs. 3a and 3b). In the Pacific, these AR changes are driven by a weakened mid-Holocene Aleutian Low and a northward displaced Pacific jet stream (Figs. 3e, 3f, 3i, and 3j), which are consistent with a more La-Niña-like climate state at the time (Barron and Anderson, 2011). The Atlantic AR changes are the result of a stronger Azores High and Icelandic Low dipole, consistent with pollen and alkenone-based temperature and SST reconstructions that indicate a slightly more positive North Atlantic Oscillation regime during the mid-Holocene (Figs. 3i and 3j) (Rimbu et al., 2003).

These AR responses to Holocene forcing resemble modern observed relationships between regional circulation and AR activity. In East Asia, present-day ARs are associated with an enhanced East Asian summer monsoon and strong southwesterly flow along the northwestern flank of an intensified seasonal Pacific anticyclone (Kamae et al., 2017), similar to the anomalous climate conditions in *CESM-MH*. Likewise, enhanced AR activity in Alaska today coincides with broad positive geopotential height anomalies in the North Pacific and occurs at the expense of AR landfalls farther south along the U.S. West Coast (Mundhenk et al., 2016), consistent with the northward displacement of ARs around the strengthened North Pacific High in *CESM-MH*. Similarly, just as the landfall location of ARs in Chile are controlled by variations in the strength

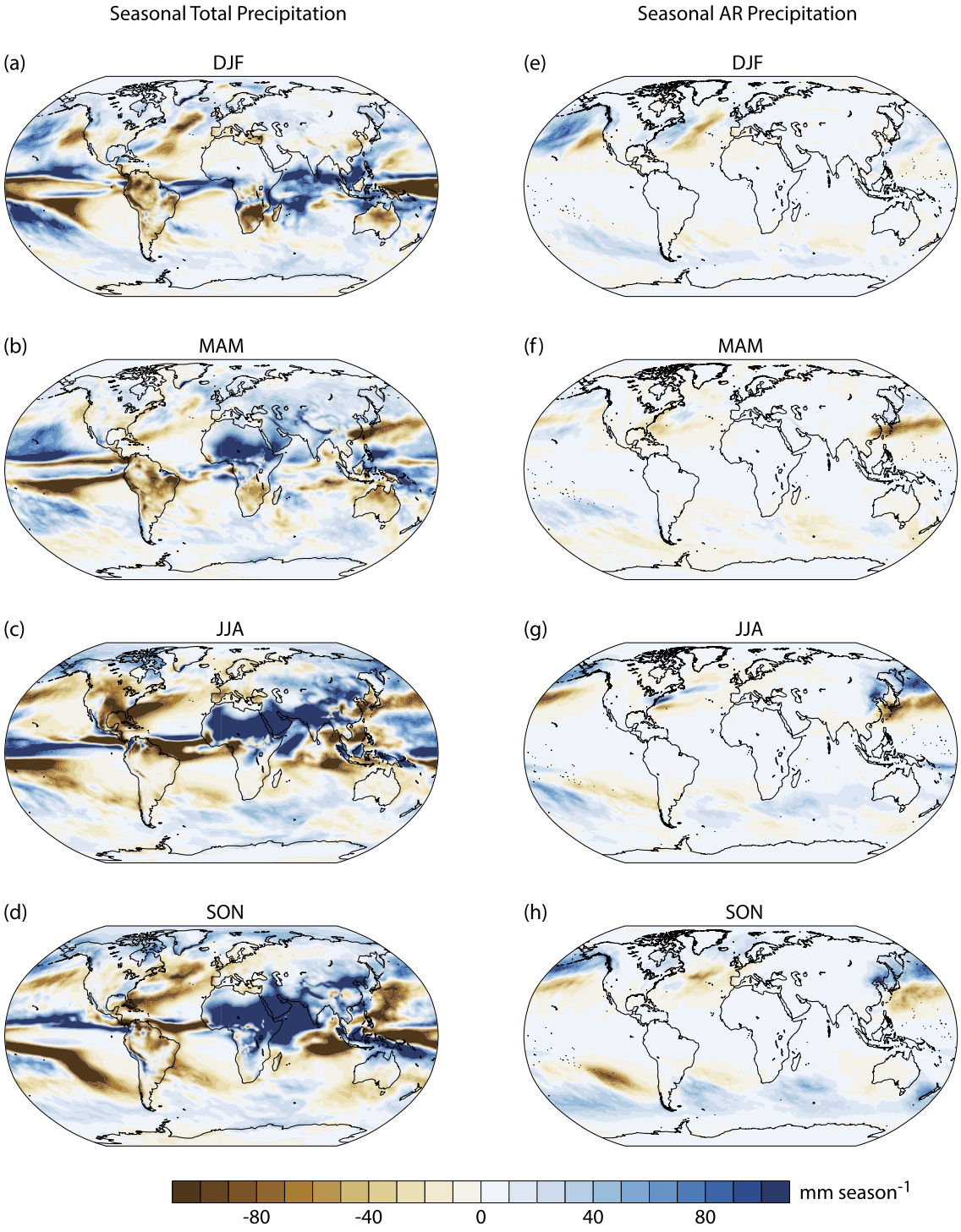

Fig. 5. (a-d) Mean change in total seasonal precipitation, and (e-h) mean change in AR-derived precipitation between CESM_MH and CESM_PI. Note, the colorbar spans −100 to 100 mm season-1 to highlight precipitation changes in the mid-latitudes.

and position of the South Pacific High today (Viale et al., 2018), a strengthened and polewards-displaced South Pacific High during the mid-Holocene enhances AR frequency in far southern Chile (south of 40°S) relative to the preindustrial climate. Likewise, enhanced mid-Holocene summer AR activity on the northwest flank of the strengthened Bermuda High resembles the primary synoptic configuration that favors most present-day ARs in the Central and Southeast U.S. (Lavers and Villarini, 2015).

The identification of ARs as an underlying synoptic mechanism responsible for past mid-latitude hydroclimate changes is consistent with and expands upon previous analyses of proxy and modeling studies of mid-Holocene climate. For example, the simulated poleward shift and increase in mid-Holocene AR frequency in East Asia (Fig. 1c) supports recent hypotheses that identify a key role for monsoon-extratropical interactions in shaping millennial-scale East Asian precipitation variability (e.g., Chiang et al., 2015). In modern-day East Asia, the insolation-driven seasonal poleward progression of the mid-latitude westerly jet promotes the northward advance of East Asian summer monsoon moisture from southern China in late spring to northern China, Korea, and

Japan in mid-to-late summer. Much of this low-latitude moisture is transported northwards in extratropic-forced atmospheric rivers (Kamae et al., 2017). Drawing an analogy to the present-day East Asian seasonal cycle, the *paleo East Asian monsoon-extratropical jet* hypothesis posits that a weakened and poleward displaced summer westerly jet during the early and mid-Holocene lengthened the monsoon rainy season in northern East Asia at the expense of regions further south (Chiang et al., 2015). Enhanced and poleward displaced AR activity is a plausible synoptic mechanism for this anomalous northward moisture transport and is consistent with a mid-Holocene wet north-dry south dipole anomaly inferred from East Asian pollen and lake records (Liu et al., 2014).

Likewise, greater AR frequency and AR-derived precipitation over the southern Andes in *CESM-EH* and *CESM-MH* relative to *CESM-PI* agrees with proxy-based inferences that extreme precipitation and flooding events have become less frequent in the region since the early Holocene (Figs. 1, 4, and S3). Geologic evidence for increased early to mid-Holocene extreme precipitation events in the southern Andes comes from a lacustrine core in southern Chile (52°S) (Lamy et al., 2010). The lacustrine core contains several terrestrial mass flow layers dated to the early/mid-Holocene which have been interpreted as evidence for heavy precipitation-driven runoff and erosion. Given that ARs account for the majority of present-day extreme precipitation events in the region (Viale et al., 2018), it is likely that increased AR activity lead to enhanced erosion and runoff during the early to mid-Holocene, consistent with the proxy interpretation.

The simulated AR responses are also consistent with and expand upon hypotheses regarding past atmospheric circulation and moisture sourcing changes in western North America. For example, mid-Holocene maxima in lake diatom oxygen isotope values ($\delta^{18}O_{diatoms}$) from the Aleutian Islands have been interpreted as evidence for the enhanced southerly advection of ^{18}O-enriched moisture (Bailey et al., 2018), which is consistent with the strong southerly moisture transport found in ARs. Indeed, atmospheric rivers exhibit distinct isotopic signatures from other precipitating systems and in some instances can conserve isotopic signals from their source (Bonne et al., 2015). Similarly, $\delta^{18}O$ records from lake sediments, glacier ice, and peat across multiple sites in mainland Alaska all exhibit their highest Holocene isotope values during the mid-Holocene (though several of these records do not extend beyond 9 ka B.P.) (Kaufman et al., 2016). While the climatic interpretations of these mainland Alaska records vary due to the complex set of processes that shape $\delta^{18}O$, enhanced transport of ^{18}O-enriched Pacific moisture from greater AR activity is a plausible explanation for the mid-Holocene $\delta^{18}O$ spike, especially given that ARs account for greater than 10% more of total Alaskan annual precipitation in the mid-Holocene simulation compared with the preindustrial simulation (Fig. 4c).

In California, simulated reductions in mid-Holocene winter AR activity are an important contributor to lower annual precipitation totals, consistent with the hypothesis of Hermann et al. (2018) (Fig. 5). In the U.S. Pacific Northwest and far southern British Columbia, the model results support the hypothesis that mid-Holocene annual precipitation totals in the region were lower, but that mid-Holocene hydroclimate seasonality was more intense (e.g. Steinman et al., 2016). Winter season AR frequency, AR precipitation, and therefore total winter precipitation in the region are greater in *CESM_MH* relative to *CESM_PI* despite overall slightly drier mid-Holocene conditions (Figs. 4 and 5). The simulated AR increases are consistent with the interpretation that relatively low mid-Holocene $\delta^{18}O$ values in closed-basin lake sediment records in the region, which are particularly sensitive to winter hydroclimate changes, reflect greater mid-Holocene winter season precipitation (Steinman et al., 2016). The result also highlights the fact that annual mean drier conditions do not necessarily reflect fewer or less intense storm systems in all seasons. Indeed, because climate proxies often have seasonal biases (for example, the proxy is especially sensitive to environmental conditions in a particular season), environmental changes in other seasons may be masked in proxy records. The simulations here suggest that overall drier mid-Holocene conditions across the Western U.S. were driven by spatially heterogenous mechanisms, with winter AR precipitation deficits contributing to drying in California and spring and summer precipitation reductions unrelated to ARs contributing to drying in portions of Oregon and Washington. This result is consistent with the large number of proxies that suggest annual mean drying in the mid-Holocene (Hermann et al., 2018), and with the set of proxies with known winter season hydroclimate sensitivity (see discussion in Steinman et al., 2016).

The sensitivity of ARs to insolation forcing suggests that AR characteristics have likely varied throughout Earth's past (e.g. Skinner and Poulsen, 2016; Lora et al., 2017), and that new insights into past hydroclimate changes may be gained by bringing AR science to bear on future paleoclimate studies. In this context, it will be important to apply a suite of AR identification and tracking algorithms to paleoclimate model data to quantify uncertainties due to algorithm design and to ensure the robustness of the AR findings (Shields et al., 2018). Additionally, these AR studies will benefit from higher model spatial resolution which may reduce AR detection biases such as the underestimation of AR frequency found in CESM (Figs. 1a and 1b) (Hagos et al., 2015). In addition to refining our understanding of past hydroclimate change, the results also place modern day AR variability into much needed context. The Holocene climate simulations indicate that AR characteristics, including frequency, moisture transport, and precipitation have all varied beyond their present-day distributions in the past. This not only highlights the sensitivity of ARs to climate forcing, but also portends future AR changes and associated impacts in response to rising future CO_2. Indeed, since the preindustrial period, several dynamic and thermodynamic changes to the climate system in response to elevated greenhouse gas warming, including greater atmospheric moisture content and poleward expansion of the Hadley Cells (IPCC, 2007), suggest that aspects of AR climatology such as track and integrated vapor transport may already be transitioning towards conditions that resemble those in the mid-Holocene.

Declaration of competing interest

The authors declare that they have no known competing financial interests or personal relationships that could have appeared to influence the work reported in this paper.

Acknowledgements

This work was supported by National Science Foundation Award 1602956, and National Science Foundation Award 1903600. The CESM project is supported by the National Science Foundation and the Office of Science (BER) of the U.S. Department of Energy. We would like to acknowledge high-performance computing support from Cheyenne (https://doi.org/10.5065/D6RX99HX) provided by NCAR's Computational and Information Systems Laboratory, sponsored by the National Science Foundation. Model data are available upon request.

Appendix A. Supplementary material

Supplementary material related to this article can be found online at https://doi.org/10.1016/j.epsl.2020.116293.

References

Albano, C.M., Dettinger, M.D., Soulard, C.E., 2017. Influence of atmospheric rivers on vegetation productivity and fire patterns in the southwestern U.S. J. Geophys. Res., Biogeosci. 122 (2), 308–323. https://agupubs.onlinelibrary.wiley.com/doi/abs/10.1002/2016JG003608.

Bailey, H.L., Kaufman, D.S., Sloane, H.J., Hubbard, A.L., Henderson, A.C.G., Leng, M.J., et al., 2018. Holocene atmospheric circulation in the central North Pacific: a new terrestrial diatom and $\delta^{18}O$ dataset from the Aleutian Islands. Quat. Sci. Rev. 194, 27–38. http://www.sciencedirect.com/science/article/pii/S0277379118303718.

Barron, J.A., Anderson, L., 2011. Enhanced Late Holocene ENSO/PDO expression along the margins of the eastern North Pacific. Quat. Int. 235 (1), 3–12. http://www.sciencedirect.com/science/article/pii/S1040618210001084.

Bartlein, P.J., Harrison, S.P., Brewer, S., Connor, S., Davis, B.A.S., Gajewski, K., et al., 2011. Pollen-based continental climate reconstructions at 6 and 21 ka: a global synthesis. Clim. Dyn. 37 (3–4), 775–802. https://doi.org/10.1007/s00382-010-0904-1. http://download.springer.com/static/pdf/753/art%253A10.1007%252Fs00382-010-0904-1.pdf?auth66=1423700886_4cf9b3b96d5d317a7665d66f0e3be12c&ext=.pdf.

Berger, A., Loutre, M.-F., Tricot, C., 1993. Insolation and Earth's orbital periods. J. Geophys. Res., Atmos. 98 (D6), 10341–10362. https://doi.org/10.1029/93JD00222.

Blamey, R.C., Ramos, A.M., Trigo, R.M., Tomé, R., Reason, C.J.C., 2017. The influence of atmospheric rivers over the South Atlantic on winter rainfall in South Africa. J. Hydrometeorol. 19, 127–142.

Bonne, J.-L., Steen-Larsen, H.C., Risi, C., Werner, M., Sodemann, H., Lacour, J.-L., et al., 2015. The summer 2012 Greenland heat wave: in situ and remote sensing observations of water vapor isotopic composition during an atmospheric river event. J. Geophys. Res., Atmos. 120 (7), 2970–2989. https://agupubs.onlinelibrary.wiley.com/doi/abs/10.1002/2014JD022602.

Carré, M., Azzoug, M., Bentaleb, I., Chase, B.M., Fontugne, M., Jackson, D., et al., 2012. Mid-Holocene mean climate in the South eastern Pacific and its influence on South America. Quat. Int. 253, 55–66. http://www.sciencedirect.com/science/article/pii/S1040618211000814.

Chiang, J.C.H., Fung, I.Y., Wu, C.-H., Cai, Y., Edman, J.P., Liu, Y., Day, J.A., Bhattacharya, T., Mondal, Y., Labrousse, C.A., 2015. Role of seasonal transitions and westerly jets in East Asian paleoclimate. Quat. Sci. Rev. 108, 111–129.

Claussen, M., Dallmeyer, A., Bader, J., 2017. Theory and Modeling of the African Humid Period and the Green Sahara. Oxford University Press.

Dallmeyer, A., Claussen, M., Wang, Y., Herzschuh, U., 2013. Spatial variability of Holocene changes in the annual precipitation pattern: a model-data synthesis for the Asian monsoon region. Clim. Dyn. 40 (11), 2919–2936. https://doi.org/10.1007/s00382-012-1550-6.

Davies, F.J., Renssen, H., Blaschek, M., Muschitiello, F., 2015. The impact of Sahara desertification on Arctic cooling during the Holocene. Clim. Past 11 (3), 571–586. https://www.clim-past.net/11/571/2015/.

Gao, Y., Lu, J., Leung, L.R., Yang, Q., Hagos, S., Qian, Y., 2015. Dynamical and thermodynamical modulations on future changes of landfalling atmospheric rivers over western North America. Geophys. Res. Lett. 42 (17), 7179–7186. https://doi.org/10.1002/2015GL065435.

Gelaro, R., McCarty, W., Suárez, M.J., Todling, R., Molod, A., Takacs, L., et al., 2017. The modern-era retrospective analysis for research and applications, version 2 (MERRA-2). J. Climate 30 (14), 5419–5454. https://doi.org/10.1175/JCLI-D-16-0758.1.

Gorodetskaya, I.V., Tsukernik, M., Claes, K., Ralph, M.F., Neff, W.D., Van Lipzig, N.P.M., 2014. The role of atmospheric rivers in anomalous snow accumulation in East Antarctica. Geophys. Res. Lett. 41 (17), 6199–6206. https://doi.org/10.1002/2014GL060881.

Guan, B., Waliser, D.E., 2015. Detection of atmospheric rivers: evaluation and application of an algorithm for global studies. J. Geophys. Res., Atmos. 120 (24), 12514–12535. https://doi.org/10.1002/2015JD024257.

Guan, B., Molotch, N.P., Waliser, D.E., Fetzer, E.J., Neiman, P.J., 2010. Extreme snowfall events linked to atmospheric rivers and surface air temperature via satellite measurements. Geophys. Res. Lett. 37 (20). https://doi.org/10.1029/2010GL044696.

Hagos, S., Leung, L.R., Yang, Q., Zhao, C., Lu, J., 2015. Resolution and dynamical core dependence of atmospheric river frequency in global model simulations. J. Climate 28 (7), 2764–2776. https://doi.org/10.1175/JCLI-D-14-00567.1.

Hermann, N.W., Oster, J.L., Ibarra, D.E., 2018. Spatial patterns and driving mechanisms of mid-Holocene hydroclimate in western North America. J. Quat. Sci. 33 (4), 421–434. https://doi.org/10.1002/jqs.3023.

Herzschuh, U., Cao, X., Laepple, T., Dallmeyer, A., Telford, R.J., Ni, J., et al., 2019. Position and orientation of the westerly jet determined Holocene rainfall patterns in China. Nat. Commun. 10 (1), 2376. https://doi.org/10.1038/s41467-019-09866-8.

Hoelzmann, P., Jolly, D., Harrison, S.P., Laarif, F., Bonnefille, R., Pachur, H.J., 1998. Mid-Holocene land-surface conditions in northern Africa and the Arabian Peninsula: a data set for the analysis of biogeophysical feedbacks in the climate system. Glob. Biogeochem. Cycles 12 (1), 35–51. https://doi.org/10.1029/97GB02733.

Hopcroft, P.O., Valdes, P.J., Harper, A.B., Beerling, D.J., 2017. Multi vegetation model evaluation of the Green Sahara climate regime. Geophys. Res. Lett. 44 (13), 6804–6813. https://doi.org/10.1002/2017GL073740.

Hurrell, J.W., Holland, M.M., Gent, P.R., Ghan, S., Kay, J.E., Kushner, P.J., et al., 2013. The community Earth system model: a framework for collaborative research. Bull. Am. Meteorol. Soc. 94 (9), 1339–1360. https://doi.org/10.1175/BAMS-D-12-00121.1.

IPCC, 2007. Climate Change 2007: The Physical Science Basis. Contribution of Working Group I to the Fourth Assessment Report of the Intergovernmental Panel on Climate Change. Cambridge University Press, Cambridge, United Kingdom and New York, NY, USA.

Kamae, Y., Mei, W., Xie, S.-P., Naoi, M., Ueda, H., 2017. Atmospheric rivers over the northwestern Pacific: climatology and interannual variability. J. Climate 30 (15), 5605–5619. https://doi.org/10.1175/JCLI-D-16-0875.1.

Kaufman, D.S., Axford, Y.L., Henderson, A.C.G., McKay, N.P., Oswald, W.W., Saenger, C., et al., 2016. Holocene climate changes in eastern Beringia (NW North America) – a systematic review of multi-proxy evidence. Quat. Sci. Rev. 147, 312–339. http://www.sciencedirect.com/science/article/pii/S027737911530144X.

Kiehl, J.T., Shields, C.A., Snyder, M.A., Zachos, J.C., Rothstein, M., 2018. Greenhouse- and orbital-forced climate extremes during the early Eocene. Philos. Trans. R. Soc. A, Math. Phys. Eng. Sci. 376, 20170085.

Kutzbach, J.E., 1981. Monsoon climate of the early Holocene: climate experiment with the Earth's orbital parameters for 9000 years ago. Science 214 (4516), 59–61. https://doi.org/10.1126/science.214.4516.59. http://www.sciencemag.org/content/214/4516/59.

Lamy, F., Kilian, R., Arz, H.W., Francois, J.-P., Kaiser, J., Prange, M., Steinke, T., 2010. Holocene changes in the position and intensity of the southern westerly wind belt. Nat. Geosci. 3, 695–699.

Lavers, D.A., Villarini, G., 2015. The contribution of atmospheric rivers to precipitation in Europe and the United States. J. Hydrol. 522, 382–390. http://www.sciencedirect.com/science/article/pii/S0022169414010208.

Liu, Z., Wen, X., Brady, E.C., Otto-Bliesner, B., Yu, G., Lu, H., Cheng, H., Wang, Y., Zheng, W., Ding, Y., Edwards, R.L., Cheng, J., Liu, W., Yang, H., 2014. Chinese cave records and the East Asia Summer Monsoon. Quat. Sci. Rev. 83, 115–128.

Lora, J.M., Mitchell, J.L., Risi, C., Tripati, A.E., 2017. North Pacific atmospheric rivers and their influence on western North America at the Last Glacial Maximum. Geophys. Res. Lett. 44 (2), 1051–1059. https://agupubs.onlinelibrary.wiley.com/doi/abs/10.1002/2016GL071541.

Mantsis, D.F., Clement, A.C., Kirtman, B., Broccoli, A.J., Erb, M.P., 2013. Precessional cycles and their influence on the North Pacific and North Atlantic summer anticyclones. J. Climate 26 (13), 4596–4611. https://doi.org/10.1175/JCLI-D-12-00343.1.

Mayle, Francis E., Power, Mitchell J., 2008. Impact of a drier early–mid-Holocene climate upon Amazonian forests. Philos. Trans. R. Soc. B, Biol. Sci. 363 (1498), 1829–1838. https://doi.org/10.1098/rstb.2007.0019.

Mbengue, C., Schneider, T., 2018. Linking Hadley circulation and storm tracks in a conceptual model of the atmospheric energy balance. J. Atmos. Sci. 75 (3), 841–856. https://doi.org/10.1175/JAS-D-17-0098.1.

Monnin, E., Indermühle, A., Dällenbach, A., Flückiger, J., Stauffer, B., Stocker, T.F., et al., 2001. Atmospheric CO_2 concentrations over the last glacial termination. Science 291 (5501), 112. https://doi.org/10.1126/science.291.5501.112.

Mundhenk, B.D., Barnes, E.A., Maloney, E.D., Nardi, K.M., 2016. Modulation of atmospheric rivers near Alaska and the U.S. West Coast by northeast Pacific height anomalies. J. Geophys. Res., Atmos. 121 (21), 12,751–12,765. https://doi.org/10.1002/2016JD025350.

Neiman, P.J., Ralph, F.M., Wick, G.A., Lundquist, J.D., Dettinger, M.D., 2008. Meteorological characteristics and overland precipitation impacts of atmospheric rivers affecting the West Coast of North America based on eight years of SSM/I Satellite Observations. J. Hydrometeorol. 9 (1), 22–47. https://doi.org/10.1175/2007JHM855.1.

Payne, A.E., Magnusdottir, G., 2015. An evaluation of atmospheric rivers over the North Pacific in CMIP5 and their response to warming under RCP 8.5. J. Geophys. Res., Atmos. 120 (21), 11,173–11,190.

Ralph, F.M., Neiman, P.J., Wick, G.A., 2004. Satellite and CALJET aircraft observations of atmospheric rivers over the eastern North Pacific Ocean during the winter of 1997/98. Mon. Weather Rev. 132 (7), 1721–1745. https://journals.ametsoc.org/doi/abs/10.1175/1520-0493%282004%29132%3C1721%3ASACAOO%3E2.0.CO%3B2.

Ralph, F.M., Dettinger, M.D., Cairns, M.M., Galarneau, T.J., Eylander, J., 2018. Defining "atmospheric river": how the glossary of meteorology helped resolve a debate. Bull. Am. Meteorol. Soc. 99 (4), 837–839. https://doi.org/10.1175/BAMS-D-17-0157.1.

Ralph, F.M., Rutz, J.J., Cordeira, J.M., Dettinger, M., Anderson, M., Reynolds, D., et al., 2019. A scale to characterize the strength and impacts of atmospheric rivers. Bull. Am. Meteorol. Soc. 100 (2), 269–289. https://doi.org/10.1175/BAMS-D-18-0023.1.

Rimbu, N., Lohmann, G., Kim, J.H., Arz, H.W., Schneider, R., 2003. Arctic/North Atlantic Oscillation signature in Holocene sea surface temperature trends as obtained from alkenone data. Geophys. Res. Lett. 30 (6). https://doi.org/10.1029/2002GL016570.

Routson, C.C., McKay, N.P., Kaufman, D.S., Erb, M.P., Goosse, H., Shuman, B.N., et al., 2019. Mid-latitude net precipitation decreased with Arctic warming during the Holocene. Nature 568 (7750), 83–87. https://doi.org/10.1038/s41586-019-1060-3.

Rutz, J.J., Steenburgh, W.J., Ralph, F.M., 2014. Climatological characteristics of atmospheric rivers and their inland penetration over the western United States. Mon. Weather Rev. 142 (2), 905–921. https://doi.org/10.1175/MWR-D-13-00168.1.

Rutz, J.J., Shields, C.A., Lora, J.M., Payne, A.E., Guan, B., Ullrich, P., et al., 2019. The atmospheric river tracking method intercomparison project (ARTMIP): quantifying uncertainties in atmospheric river climatology. J. Geophys. Res., Atmos. 124, 13777–13802.

Schneider, T., Bischoff, T., Haug, G.H., 2014. Migrations and dynamics of the intertropical convergence zone. Nature 513, 45. https://doi.org/10.1038/nature13636. Review Article.

Shields, C.A., Kiehl, J.T., 2016. Atmospheric river landfall-latitude changes in future climate simulations. Geophys. Res. Lett. 43 (16), 8775–8782. https://doi.org/10.1002/2016GL070470.

Shields, C.A., Rutz, J.J., Leung, L.Y., Ralph, F.M., Wehner, M., Kawzenuk, B., et al., 2018. Atmospheric river tracking method intercomparison project (ARTMIP): project goals and experimental design. Geosci. Model Dev. 11 (6), 2455–2474. https://www.geosci-model-dev.net/11/2455/2018/.

Skinner, C.B., Poulsen, C.J., 2016. The role of fall season tropical plumes in enhancing Saharan rainfall during the African Humid Period. Geophys. Res. Lett. 43 (1), 349–358. https://doi.org/10.1002/2015GL066318.

Steinman, B.A., Pompeani, D.P., Abbott, M.B., Ortiz, J.D., Stansell, N.D., Finkenbinder, M.S., et al., 2016. Oxygen isotope records of Holocene climate variability in the Pacific northwest. Quat. Sci. Rev. 142, 40–60. http://www.sciencedirect.com/science/article/pii/S0277379116301238.

Viale, M., Valenzuela, R., Garreaud, R.D., Ralph, F.M., 2018. Impacts of atmospheric rivers on precipitation in southern South America. J. Hydrometeorol. 19, 1671–1687.

Viau, A.E., Gajewski, K., 2009. Reconstructing millennial-scale, regional paleoclimates of boreal Canada during the Holocene. J. Climate 22 (2), 316–330. https://doi.org/10.1175/2008JCLI2342.1.

Wanner, H., Beer, J., Bütikofer, J., Crowley, T.J., Cubasch, U., Flückiger, J., et al., 2008. Mid- to Late Holocene climate change: an overview. Quat. Sci. Rev. 27 (19), 1791–1828. http://www.sciencedirect.com/science/article/pii/S0277379108001479.

Zhu, Y., Newell, R.E., 1998. A proposed algorithm for moisture fluxes from atmospheric rivers. Mon. Weather Rev. 126 (3), 725–735. https://doi.org/10.1175/1520-0493(1998)126<0725:APAFMF>2.0.CO;2.